# Dry Transfer of van der Waals Crystals to Noble-Metal Surfaces to Enable Characterization of Buried Interfaces

Andrey Krayev<sup>1</sup>, Connor S. Bailey<sup>2</sup>, Kiyoung Jo<sup>3</sup>, Shuo Wang<sup>4</sup>, Akshay Singh<sup>5</sup>, Thomas Darlington<sup>6</sup>, Gang-Yu Liu<sup>4</sup>, Silvija Gradecak<sup>5</sup>, P.James Schuck<sup>6</sup>, Eric Pop<sup>2</sup>, Deep Jariwala<sup>3</sup>\*

- 1. Horiba Scientific, Novato, CA 94949, USA
- 2. Department of Electrical Engineering, Stanford University, Stanford, CA, 94305, USA
- 3. Department of Electrical and Systems Engineering, University of Pennsylvania, Philadelphia, PA 19104, USA
- 4. Department of Chemistry, University of California, Davis, CA 95616, USA
- 5. Department of Materials Science and Engineering, Massachusetts Institute of Technology, Cambridge, MA, 02139 USA
- 6. Department of Mechanical Engineering, Columbia University, New York, NY, 10027, USA

#### **ABSTRACT**

Two dimensional (2D) transition metal dichalcogenides (TMDCs) have been explored for many optoelectronic applications. Most of these applications require them to be on insulating substrates. However, for many fundamental property characterizations, such as mapping surface potential or conductance, insulating substrates are non-ideal as they lead to charging and doping effects, or impose the inhomogeneity of their charge environment on the atomically-thin 2D layers. Here, we report a simple method of residue-free dry transfer of 2D TMDC crystal layers. This method is enabled via noble metal (gold, silver) thin films and allows comprehensive nanoscale characterization of transferred TMDC crystals with multiple scanning probe microscopy (SPM) techniques. In particular, intimate contact with underlying metal allows efficient tip-enhanced Raman scattering (TERS) characterization, providing high spatial resolution (< 20 nm) for Raman spectroscopy. Further, scanning Kelvin Probe Force microscopy (KPFM) allows high resolution mapping of surface potential on transferred crystals, revealing their spatially varying structural and electronic properties. The layer-dependent contact potential difference (CPD) is clearly observed and explained by charge transfer from contacts with Au and Ag. The demonstrated sample preparation technique can be generalized to probe many different 2D material surfaces, and has broad implications in understanding of the metal contacts and buried interfaces in 2D materialsbased devices.

**Keywords**: van der Waals materials, transition metal dichalcogenides, near-field, buried interfaces, Raman spectroscopy, TERS

<sup>\*</sup>Corresponding Author. Email: dmj@seas.upenn.edu

### Introduction

The advent of layered two-dimensional (2D) crystals with van der Waals interlayer interactions has opened up new research avenues in materials, surface science, as well as condensed matter physics and device engineering. While 2D materials such as graphene and transition metal dichalcogenides (TMDC) have been extensively studied both for fundamental science and device applications, a majority of these studies have occurred on insulating substrates, which are critical for field-effect devices. However, most practical 2D devices tend to also have metal interfaces (e.g. contacts), which are a subject of much debate and numerous studies have been dedicated to understand this interface. To date, little is known about this buried interface using direct microscopic and spectroscopic measurements. Even less is known in the context of 2D materials where the band structure changes as a function of thickness and the interfaces are highly sensitive to contamination. Metal contacts to semiconductors are ubiquitous in all solid state devices and more recently have been critical for the case of TMDCs for ultrathin photovoltaics. Thorough understanding of physical phenomena occurring at metal/2D semiconductor interfaces is therefore not only a matter of pure academic interest, but is an equally important problem for prospective applications.

Direct exfoliation using an adhesive tape method from bulk crystals and polymer-assisted transfer of chemical vapor deposition (CVD)-grown crystals are two of the most popular techniques for TMDC sample preparation and transfer. However, both suffer from the same unavoidable problem, i.e. the introduction of polymer contamination. This can significantly alter the distribution of the surface potential and even topography, when puddles of low-molecular weight polymer spread across the sample surface with time, compromising the quality of the contacts and heterojunctions.<sup>24</sup> An alternative, cleaner method was introduced recently,<sup>25</sup> wherein a thin gold film is evaporated onto bulk TMDC crystals, using it to preferentially exfoliate monoand few-layers, then etched away in KI/I<sub>2</sub> solution, thus avoiding polymer contamination. Similarly evaporated Ni thin films have been used to exfoliate wafer scale monolayers from multilayer films. 26 Despite obvious advantages of such a method, the etching solution and some atomic metal residue are unavoidable. Another interesting technique was published recently on freshly evaporated, smooth gold films-assisted exfoliation of large, hundreds of microns across, mono- to few-layer TMDC crystals.<sup>27</sup> Scotch-tape assisted exfoliation from bulk TMDC crystals was a crucial step in this reported methodology. While the reported approach enables intimate contact between freshly cleaved surface of the TMDC crystal and the gold substrate across large areas, it would be inapplicable for the transfer of the CVD grown single-to-few-layer TMDC crystals, since it becomes increasingly difficult to attain intimate mechanical contact (1-2Å) across large areas between two rigid surfaces such as Si wafers. Further, the peeling/exfoliation is this case is critically dependent on surface contamination of Au film and interlayer interactions between the van der Waals materials and top layer in contact with Au.

In this work, we propose a facile method, also based on use of noble metals such as silver or gold, which is suitable for transfer of CVD-grown TMDCs, regardless of layer thickness or

preparation type. The transferred TMDC samples on noble metals have pristine interfaces on both sides, i.e. the contact with noble metal as well as the exposed interface. This allows the characterization of transferred TMDCs and their buried interface with few nm-scale resolution using scanning probe microscopy (SPM) techniques. Further, being in close proximity with a noble metal such as Au or Ag, we can use plasmonic probe tips to perform near-field spectroscopy characterization via tip-enhanced Raman spectroscopy (TERS). Our results demonstrate that the noble metal-based one step transfer process produces atomically clean buried interfaces and suggests that the charge transfer between noble metals and TMDCs can vary significantly depending on the metal and number of layers of the TMDC.

## **Experimental:**

TMDC crystals, both WSe<sub>2</sub><sup>28</sup> and MoS<sub>2</sub><sup>29</sup> were grown via the standard powder precursor based CVD techniques. Gold deposition via thermal evaporation was performed in a model DV502-A high vacuum evaporator, (Denton Vacuum Inc., Moorestown, NJ); e-beam assisted gold deposition was done in a model PVD-75 e-beam evaporator (Kurt Lesker). All scanning probe characterizations including Atomic Force Microscopy (AFM), Kelvin Probe Force Microscopy (KPFM), Far-field Raman spectroscopy and Tip Enhanced Raman Spectroscopy (TERS) characterizations were performed in either XloRA-Nano or LabRam-Nano AFM-Raman systems (Horiba Scientific). All other details are discussed in Supporting Information.

#### **Results and Discussion:**

To perform this study, we investigated a set of TMDC samples (here WSe<sub>2</sub><sup>28</sup> and MoS<sub>2</sub><sup>29</sup>) grown by CVD. Details of the synthetic procedures can be found in the corresponding section of Supporting Information. All data shown in the figures below is based on WSe<sub>2</sub> hence all references to TMDC in the figures is for WSe<sub>2</sub> but can be generalized to MoS<sub>2</sub> and possibly other TMDCs as well. The data on MoS<sub>2</sub> is presented in the Supporting Information. The step-by-step procedure of the proposed noble-metal-assisted transfer method is shown in Figure 1a (full process) and Figure 1b (cross section of initial and final stage of the samples). First, a thin gold (100 nm) or silver film (55 nm Ag covered by 50 nm Au) is directly thermally deposited on top of the CVD-grown TMDC crystals on the SiO<sub>2</sub>/Si substrate (carrier wafer) without any pretreatment. Our preference for thermal evaporation is because it is known to be less detrimental and less likely to introduce defects as compared to e-beam evaporation. 30-31 Following evaporation, a piece of silicon wafer (transfer wafer) is glued to the noble metal film using a thin layer of thermal epoxy (Epo-Tek 375, Epoxy Technology). After the epoxy layer cures and achieves its final hardness, the top silicon piece is peeled upwards, which results in stripping of the gold/silver film together with the TMDC crystals from the substrate. This epoxy based peeling procedure has been discussed in detail in prior publications.<sup>23, 32</sup> It is worth noting that in this multilayer stack, the adhesion at the epoxy-gold and TMDC-gold interface is stronger compared to the SiO<sub>2</sub>-gold, TMDC-SiO<sub>2</sub> and TMDC-TMDC interface (for the case of bilayer and thicker flakes). Hence this peeling and transfer process works as intended.

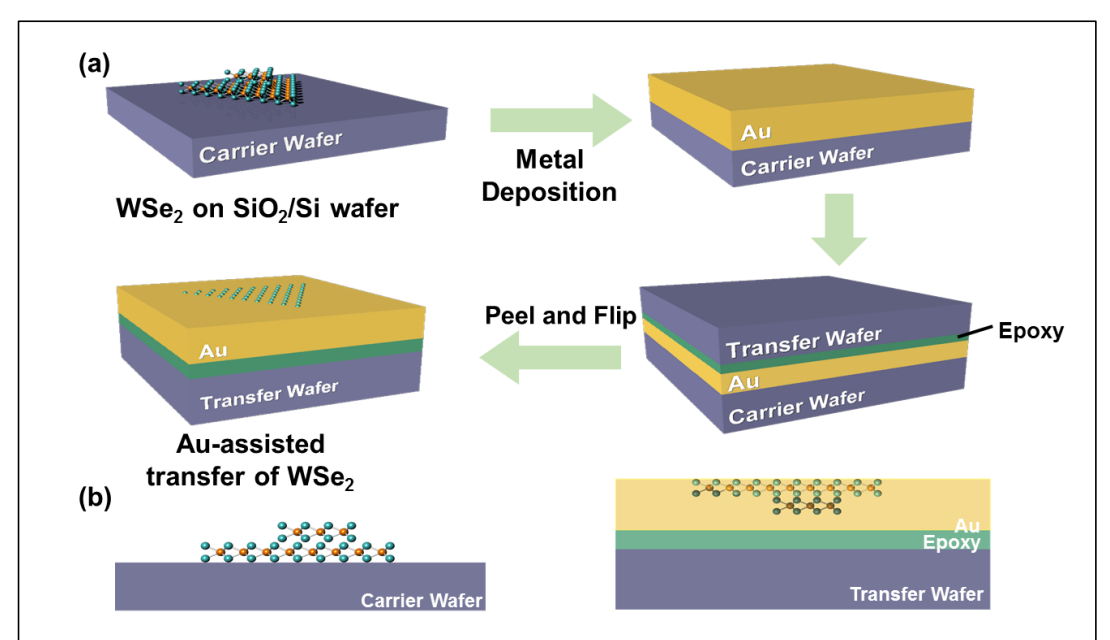


Figure 1. (a) Step-by-step scheme of gold (silver) –assisted transfer of CVD-grown TMDC crystals from the original  $SiO_2/Si$  carrier wafer onto a transfer wafer by use of thermal epoxy as the bonding layer. (b) Cross-sectional view of the samples before and after transfer.

The resulting samples after peeling were characterized using multi-mode SPM comprising of scanning Kelvin Probe Force microscopy (KPFM) analysis cross-correlated with tip-enhanced Raman scattering (TERS) mapping (Figure 2a). 12, 16, 33 As a result of this one-step transfer and peeling process, we obtained samples with topography seen in Figure 2b where TMDC crystals embedded into the gold layer were exposed on the side originally facing the SiO<sub>2</sub> substrate. The RMS roughness on the TMDC is 0.44 nm whereas on the Au is 0.43 nm. This indicates that both surfaces are equally smooth and adapt to the smoothness of the wafer on which they are deposited. We observed a number of interesting heterogeneities that varied depending on specific TMDC. In the following we discuss in-depth results obtained on WSe<sub>2</sub> transferred with gold and silver and will compare them to the results obtained on gold-transferred MoS<sub>2</sub> presented in the Supporting Information.

For the case of CVD-grown WSe<sub>2</sub> samples, after transfer we observed shallow topography and a number of features in contact potential difference (CPD) maps (Fig. 2c). Primarily, in the center of the triangular crystals we frequently observed perfectly concentric triangular areas with lower surface potential (about 70-100 mV lower) as seen in Fig. 2c. Such concentric triangular features most probably correspond to a thicker region of second or higher number of layers nucleating from the center of the first layer which often appears in large CVD-grown TMDC crystals.<sup>28</sup> Note that because the few-layer thick inner triangle faces "down" into the noble metal layer, the topography is flat, but changes are still measurable using CPD. In addition to the central island with decreased value of CPD, we observed irregularly-shaped fractal features that also showed lower value of the surface potential compared to adjacent area, though the value of the CPD drop was somewhat smaller (~15-20 mV) compared to the central island (70-100 mV). Such fractal or dendrite shaped features that may appear at certain growth conditions have been

experimentally observed and theoretically explained earlier.<sup>34</sup> Our results in Figure 2 suggest that even though topography shows no noticeable features, the atomically-thin nature of the semiconductor allows "peering through" the top layer via electrostatic potential interactions, to image the potential of the buried bi(multi)layers on the first grown WSe<sub>2</sub> layer.

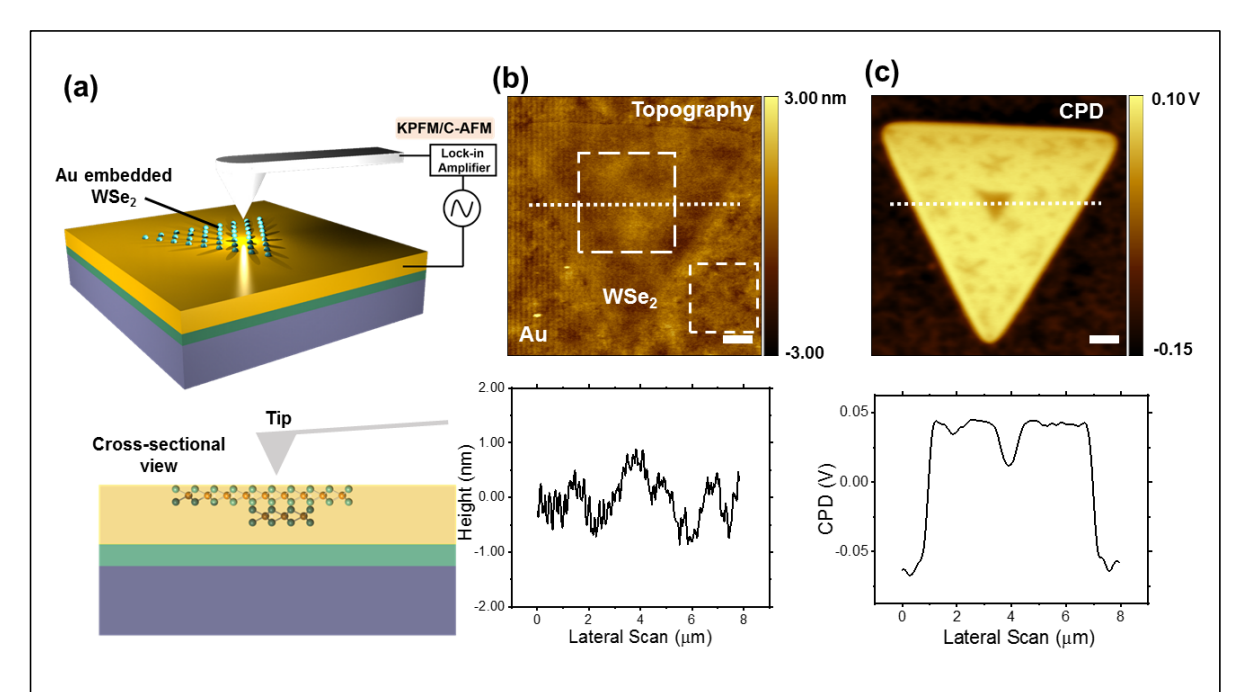


Figure 2. (a) Isometric view of schematic of measurement setup (top) and cross-sectional view (bottom). (b) Topography image of a WSe2 triangular crystal transferred with Au showing flat topography (RMS roughness  $\sim$ 0.44 on both Au and WSe2 on Au) with a faint triangular outline. Bottom shows a line-cut profile corresponding to the white line in the top image, showing little variation in topography across the TMDC and Au interface. (c) Concurrently acquired CPD image of the same TMDC triangle showing a sharp contrast between the Au substrate and the WSe2 region. Additional contrast of bilayer islands or contaminants buried underneath the monolayer are also visible. Bottom panel shows a line cut profile shown by the same dashed white line, which shows reduced surface potential for the central triangular bilayer island, as well as other irregular dendritic features interspersed across the surface. Inset scale bars in (b) and (c) are 1  $\mu$ m.

A unique feature of these transferred samples<sup>28,29</sup> is that TMDC crystals are naturally in very close proximity to plasmonic metal surfaces. Therefore, the use of a plasmonic TERS probe provides us with a capability to acquire topography, surface potential, and Raman spectroscopy information from the same sample area with the same probe at < 20 nm spatial resolution. The TERS map collected around the central triangular and fractal features showed significantly different Raman response from locations with decreased values of the surface potential (Fig. S1), therefore confirming that the chosen characterization techniques can adequately address nanoscale heterogeneities in transferred samples.

Based on our successful transfer and nanoscale characterization of the first batch of samples, we perform follow-up experiments aiming to track the changes occurring as a result of transfer on the same WSe<sub>2</sub> crystal. We performed comparative measurements on a representative CVD-grown

WSe<sub>2</sub> crystal that featured a tri-layer core in the center and several small bilayer islands of both fractal and perfectly triangular shape. Topography and CPD images of the as-grown crystal are shown in Figures 3a and 3b, respectively. The core triangle and bilayer islands of the as-grown crystal on the SiO<sub>2</sub>-Si substrate showed a higher surface potential compared to the monolayer part. The monolayer nature of the majority of the crystal was confirmed both by topography and the presence of a strong photoluminescence (PL) peak at  $\sim$ 770 nm ( $\sim$ 1.61 eV), acquired before transfer (Figure S2 in Supporting Information).

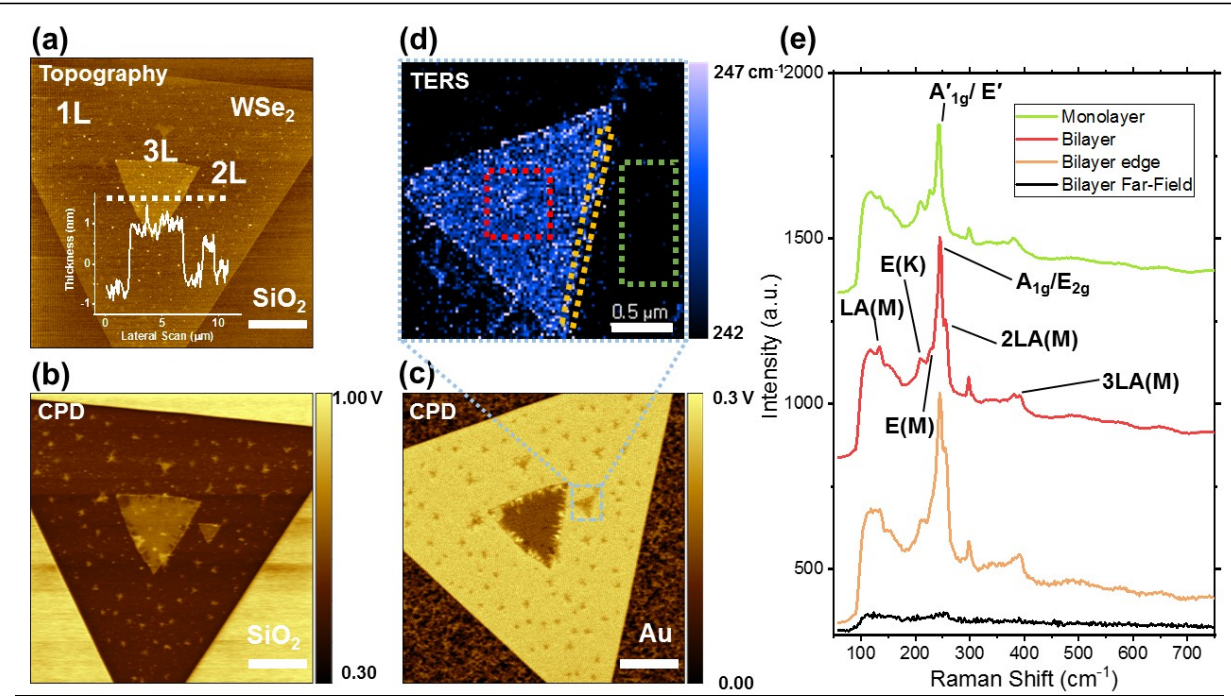


Figure 3. (a) Topography of an as-grown crystal on  $SiO_2$  and (b) corresponding CPD data. The topography analysis clearly shows mono-, bi- and tri-layer height of the various islands on  $SiO_2$  while the CPD map shows higher positive potential for  $SiO_2$  than monolayer  $WSe_2$ . The higher or more positive potential of bilayer and tri-layer vs. monolayer are also clearly visible. (c) CPD map of same portion of sample after Au-assisted transfer showing a flip in sign of relative surface potential difference between flake and substrate as well as between the mono-and multi-layer areas. (d) TERS map of blue dashed square in (c) showing higher TERS signal from bilayer island than from monolayer. The map shows average peak position of complex peak in 200-265 cm<sup>-1</sup> range (the map indicates of the average of peak position of the complex peak at each point), which efficiently reflects the intensity of the 2LA(M) peak relative to main  $A_{1g}/E_{2g}$  band. (e) Averaged TERS spectra from the monolayer part (green), inner area of the bilayer (red) and the edges of the bilayer island (orange). Black spectrum is the far-field Raman signal collected when the tip was oscillating about 25-30 nm away from the surface, with the same integration time as the TERS spectra, clearly evidencing strong TERS enhancement and the lack of any noticeable enhancement effect purely from the gold substrate. Inset scale bars in (a), (b) and (c) are 5  $\mu$ m and 500 nm in (d).

After gold assisted transfer, the CPD image looked very similar to the one shown in Figure 2, where the overall CPD of the WSe<sub>2</sub> crystal was more positive in value compared to the adjacent gold, while bi- and tri-layer islands showed lower surface potential (210 mV for bi-, 140 mV for tri-layer) compared to the adjacent monolayer (270 mV) (Figure 3c). The origin of this behavior of the CPD signal will be elaborated further in the discussion section. The TERS map collected

over one of such buried bilayer region of the triangular crystal in Figure 3d showed increased intensity of longitudinal acoustic modes LA(M), 2LA(M) and 3LA(M) in the Raman spectra compared to the adjacent monolayer (Figure 3e), which is not surprising, taking into account that these LA modes are closely associated with defects as has been reported in literature.<sup>35</sup> It is important to note that all observed peaks in the TERS spectra of gold-transferred WSe<sub>2</sub> showed a significant red shift ~8 cm<sup>-1</sup> as compared to literature precedent.<sup>36</sup> Even though a systematic study of the origins of observed red shift is beyond the scope of this manuscript, we can speculate that this shift of Raman bands in gold-transferred WSe<sub>2</sub> crystals may be caused by intrinsic bonding or interface strain related phenomenon, for example Au-Se physical bonding interaction or the inevitable mechanical stress in WSe<sub>2</sub> that may appear in the process of gold deposition and subsequently during TMDC removal from SiO2. We rule out large charge transfer induced hole doping as discussed below which typically results in small blue shifts.<sup>37</sup> We also rule out SERS or similar effects since we measure both near-field and far-field Raman signals for comparison. The far-field signal (black spectrum in Fig. 3 e) is acquired with the tip significantly ( $\sim$ 25-30 nm) away from the sample which does not show any noticeable Raman enhancement effect. Additional farfield spectra on Au and Ag are shown in Supporting information Figure S8.

We also note that the overall intensity of TERS spectra decreases as the mapping progresses, as compared to mechanically exfoliated samples (See Supporting information Figure S7) . This may be an indication of presence of some growth-related contaminant at the SiO<sub>2</sub>-WSe<sub>2</sub> interface which remains on the exposed surface of transferred crystal and aggregates at the apex of the TERS probe, corroding the chemically less stable Ag, causing decrease in its efficiency.  $^{38-39}$  We further note that our CPD and TERS observations in Figure 3 were reproducible across other samples. TERS signals of the bi- and tri-layer islands were qualitatively similar with minor differences. As was noted above, bilayer islands featured increased intensity of peaks associated with LA(M) phonons, and slight blue shift of E(M) and E(K) modes. Similar observations were made in the central tri-layer island, with even stronger increase of the intensity of 2LA(M) peak (Figure S1). It is interesting to note that we did not observe any PL in crystals transferred to gold, even though the Raman bands were strongly enhanced in our TERS spectra. We attribute this to the immediate proximity and therefore strong electronic coupling of WSe<sub>2</sub> to the metal substrate which provides a channel for non-radiative decay of excitons.

Based on the above results, it was important to understand whether this transfer process is limited to gold only or it can be extended to other noble metals such as silver. Silver (Ag) is a desirable metal for a number of reasons: first, it has a significantly lower work-function compared to gold<sup>40</sup> and therefore provides certain flexibility in terms of engineering desired electronic properties of the metal-TMD interface. Second, by alloying silver and gold one can gradually change the work-function of the substrate from 5.1 eV in case of pure polycrystalline gold to 4.3 eV for pure polycrystalline silver.<sup>40-41</sup>

Similar to the case of Au-assisted transfer, we thermally deposited 55 nm of Ag followed by 50 nm of Au (to prevent silver degradation in ambient conditions) onto the CVD-grown WSe<sub>2</sub> and stripped the crystals following the procedure described above. The transferred regions are shown in Figure 4. CPD profile (Figure 4a) and TERS characterization (Figure 4b) of the Ag-transferred

WSe<sub>2</sub> crystals revealed a number of unexpected differences compared to the crystals that were transferred using Au. First, immediately after the transfer the value of the CPD of WSe<sub>2</sub> monolayer crystals was higher relative to the Ag substrate, taking into account that the Fermi level of Ag should be higher than of WSe<sub>2</sub>. Second, the CPD of the monolayer part of crystals transferred with Ag was observed to have greater spatial non-uniformity in CPD as compared to the case of transfer using Au. This could likely be the result of polycrystalline nature of silver film and significant difference of the work-function of silver for different crystalline facets. Alternatively, silver being much more chemically active compared to gold might react with local contaminants on the surface of WSe<sub>2</sub> crystals, which would cause inevitable change in the local CPD value. Another interesting feature was the fact that the CPD of the multilayer islands (~100 mV) proved to be more positive (greater than) compared to adjacent monolayers (30 mV), unlike the case of the crystals transferred with Au. The details of work function change and doping are elaborated in the discussion below.

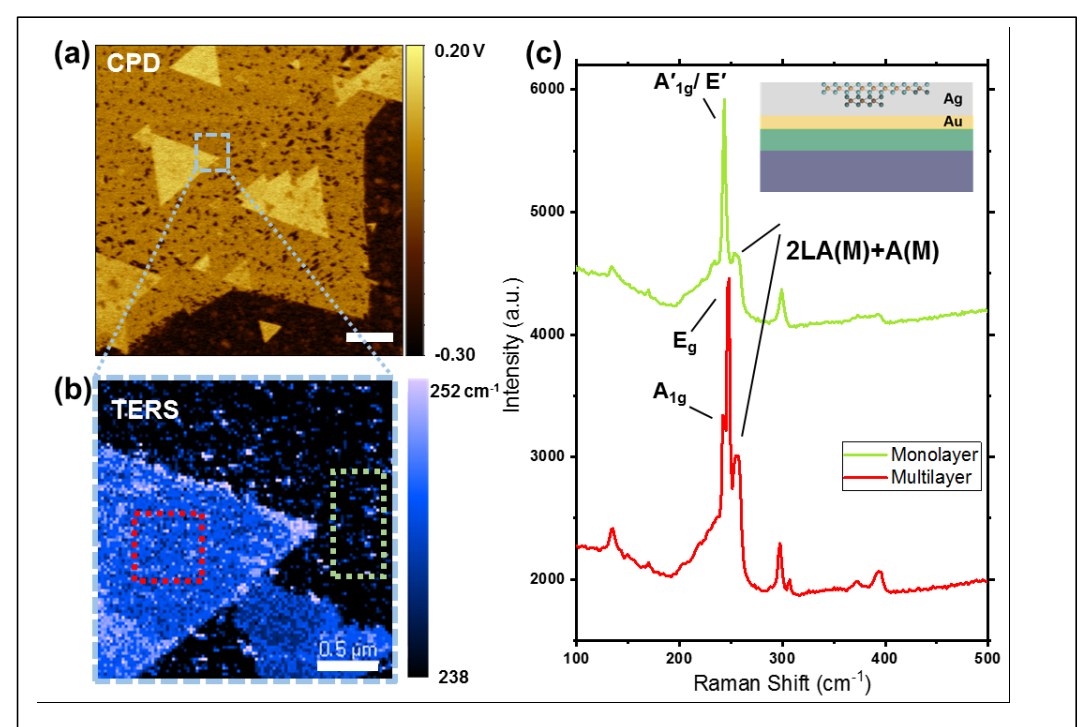


Figure 4. (a) CPD image of a WSe<sub>2</sub> crystal transferred with silver immediately after stripping (scale bar = 5  $\mu$ m) (b) TERS map corresponding to peak position of complex peak within 200-260 cm<sup>-1</sup> range in spectra shown in (c). The map indicates the average of peak position of the complex peak at each point. (c)- averaged TERS spectra from multilayer (red) and monolayer (green) parts of the crystal.

The TERS response (633 nm pump laser) of Ag-transferred WSe<sub>2</sub> was also somewhat different from the case of Au: first, we observed a fairly intense peak at 299 cm<sup>-1</sup>, which softens to 297 cm<sup>-1</sup> for multilayer islands and corresponds to the 295 cm<sup>-1</sup> peak reported previously<sup>16</sup> in WSe<sub>2</sub> crystals exfoliated on silver. The second interesting feature was a strong split of the  $E_g$  and

 $A_{1g}$  modes in multilayer islands, with  $A_{1g}$  peak position shifting to 248 cm<sup>-1</sup> from 243 cm<sup>-1</sup> of the partially overlapping E'/ $A_1$ ' peak in the case of monolayer, which has also been reported earlier.<sup>36</sup>

To further investigate the nature of the interface and generalize this transfer technique, we applied it to CVD-grown crystals of MoS<sub>2</sub> on SiO<sub>2</sub>/Si<sup>29</sup> (Figures S4-S6) in the Supporting Information, wherein the Au was sputter-deposited and thermally evaporated thereby elucidating subtle differences in the buried interface in different metal evaporation schemes. Our experiments suggest that thermally evaporated samples lead to clear observation of resonant Raman as opposed to sputtered samples suggesting higher crystalline quality of the buried TMDC interface. A detailed comparison will be subject of a separate study. In addition, Au-assisted transfer was applied not only to CVD-grown TMDCs, but also to directly exfoliated TMDCs (Figure S7 in Supporting Information). In particular, exfoliated WSe<sub>2</sub> by the adhesive-tape method, was successfully flipped through the Au-assisted transfer. The CPD value reaches the maximum at monolayer and gradually decreases as the layer becomes thicker, which corresponds well to the result of transferred CVD-grown WSe<sub>2</sub> discussed above.

Overall, our proposed transfer approach is proven to be very general and applicable across a broad spectrum of metal deposition techniques and TMDC types. Subtle differences and variation between TMDCs and metal deposition techniques can be explained by level of contamination, surface oxidation and bonding between the chalcogen and the noble metal, as detailed in the Supporting Information.

Buried electronic interfaces in 2D materials and metal-semiconductor contacts have been the subject of much debate with numerous research papers and review articles being published. However, issues such as the extent of charge transfer between the two, chemical stability of the contact and band bending are still far from clear. Our study shows that these quantities can be directly measured and imaged using a scanning probe if the interface is clean and flat which is enabled by our transfer technique (Figure 5a). From interpretation of our CPD data, we note that the CPD contrast in as-grown and transferred samples cannot be explained solely by variations of the Fermi level in mono- and multi-layered parts of the TMDC crystals, the number of layers, and correspondingly the thickness of the crystal should also play an important role. Purely electrostatic considerations suggest that the close proximity of metals to semiconductors also leads to charge transfer and formation of depletion regions. <sup>15, 42</sup>

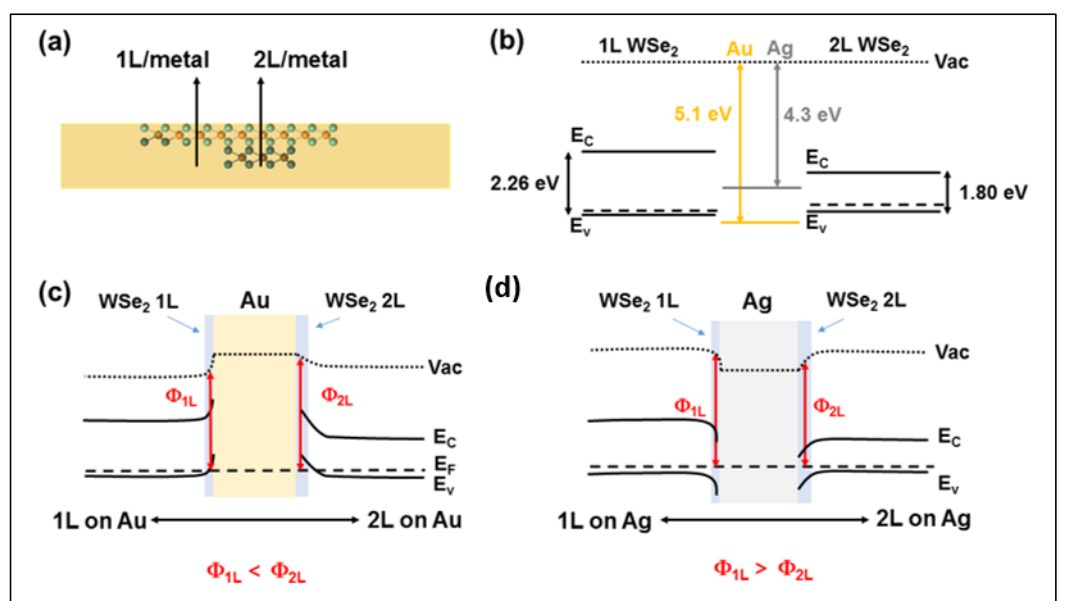


Figure 5 (a) Schematic cross-section of the WSe<sub>2</sub> embedded in Au layer with arrows showing directions along which band diagrams have been drawn. (b) Band alignments of monolayer (1L) and bilayer (2L) WSe<sub>2</sub> with that of Au and Ag. (c), (d) Projected equilibrium band diagrams on Au (c) showing Ohmic band alignment and on Ag (d) showing Schottky band alignment.

Taking all this into account, we can interpret our CPD data on three different substrates, namely SiO<sub>2</sub>, Au, and Ag as follows. For the case of as-grown WSe<sub>2</sub> on SiO<sub>2</sub> substrate, the oxide is known to have fixed positive charge. <sup>43-44</sup> This fixed positive charge is screened by the WSe<sub>2</sub> monolayer as it grows on it. Therefore, the CPD signal drops to a smaller positive value. Then as the bilayer (of same orientation) grows on the monolayer, the band gap substantially changes (reduces). As per the literature precedent of band gap evolution in WSe<sub>2</sub> as a function of layer thickness, <sup>45-46</sup> the conduction band goes down significantly and the valence band is almost unaffected, <sup>47</sup> which forms a type II alignment (Figure 5b). <sup>46, 48-49</sup> But the doping level in the flake <sup>50-51</sup> must remain the same so the Fermi level moves down. As a consequence, the work function for the bilayer goes up and the CPD value rises to be more positive. The same effect occurs for the trilayer except the jump is smaller, as the rate of gap reduction reduces with increasing thickness. <sup>45-46</sup>

When one deposits Au on the TMDC, the Au forms a very intimate contact, both physically and electronically with the TMDC. Au has a large work function (5.1 eV for polycrystalline gold<sup>40</sup>) and therefore forms an Ohmic contact with p-doped WSe<sub>2</sub>.<sup>48, 52</sup> Thus, the WSe<sub>2</sub> in close proximity to Au will be under hole accumulation (positive charge) and hence the CPD rises compared to the Au substrate and reaches 270 mV (Figure 5c). As the WSe<sub>2</sub> thickness increases, the band gap diminishes and Fermi level goes further down. However, the electronic contact remains Ohmic in nature and WSe<sub>2</sub> stays under accumulation (positive charge) except now the positive charge starts getting screened by increasing number of layers, causing less band bending and corresponding higher work function. Thus there is a drop in CPD, which is defined as

$$V_{CPD} = \frac{\Phi_{tip} - \Phi_{sample}}{q}$$

where  $\Phi$  is the respective work function and q is the elementary charge.

The case of Ag is conceptually similar to Au, except Ag has much lower work function than Au, forming a Schottky contact instead of Ohmic and thus causing hole depletion in the WSe<sub>2</sub>. This leads to lower CPD of WSe<sub>2</sub> (30 mV) compared to that of Au-transferred WSe<sub>2</sub> (270 mV) (Figure 5d). Further, with increasing thickness, a decrease in the Fermi level occurs. This is due to band gap change (reduction)<sup>47</sup> which results in reduction of the work function to cause further increase of CPD value in a bilayer and thicker regions, compared to that of a monolayer.

Based on the above results and discussion we believe that our noble metal-assisted transfer technique for TMDCs helps deepen our understanding of the metal/TMDC buried interface. In particular, it informs us that the interface contact potential is highly sensitive and depends not only on the number of layers of TMDC but also the deposition conditions (see Supporting Information S4-S6). Further, even though the TMDC layers can act as impenetrable atomically-thin barriers, their contact or junction with underlying media leaves a surface potential fingerprint which can be detected by KPFM and TERS, opening the door to sub-surface characterization of novel heterostructures and devices.

#### Conclusions:

In summary we demonstrate a robust, simple and contamination-free transfer technique of CVD-grown TMDC crystals to metallic (gold or silver) substrates. The sample surfaces produced by this technique show smooth topography (RMS roughness = 0.44 nm) making them ideal for plasmonic/conductive tip based SPM and TERS characterization. Cross-correlated CPD and TERS characterization of CVD-grown WSe<sub>2</sub> crystals showed that islands of bi- and tri-layers buried under the monolayer showed significantly different value of the surface potential compared to the adjacent monolayer, suggesting strong electronic coupling to the underlying metal, while TERS spectra of these thicker islands featured increased intensity of LA phonon modes at the M point, which in turn is an indication of the increased defect concentration.

Our transfer method seems to be particularly useful for investigation of air and moisture sensitive 2D materials like tellurides, perovskites, niobium and tantalum chalcogenides or even black phosphorus. Gold/silver deposited on top of exfoliated or CVD-grown crystals can serve as a protection barrier, thereby allowing sample exposure to characterization for barely minutes if not seconds. This presents a unique advantage that can open up new avenues for sample analysis and characterization for atomically thin materials.

# **Supporting Information**

The supporting information is available free of charge on the ACS Publications website.

Synthesis method of CVD-grown WSe<sub>2</sub> and MoS<sub>2</sub>, metal deposition, topography and PL spectrum of as-grown WSe<sub>2</sub> crystal, CPD and TERS mapping of WSe<sub>2</sub> after Au and Ag-assisted transfer; CVD-grown MoS<sub>2</sub> after Au-assisted transfer; direct exfoliated WSe<sub>2</sub> after Au-assisted transfer.

## Acknowledgements

This work was carried out in part at the Singh Center for Nanotechnology at the University of Pennsylvania and at the Stanford Nanofabrication Facility, which are supported by the National Science Foundation (NSF) National Nanotechnology Coordinated Infrastructure Program grant NNCI-1542153. D.J. and K.J. acknowledge primary support for this work by the U.S. Army Research Office under contract number W911NF1910109. D.J. also acknowledges support from Penn Engineering Start-up funds, National Science Foundation (DMR-1905853) and University of Pennsylvania Materials Research Science and Engineering Center (MRSEC) (DMR-1720530). C.S.B. acknowledges support from the NSF Graduate Fellowship. C.S.B. and E.P. were also supported in part by the Air Force Office of Scientific Research grant FA9550-14-1-0251, by the NSF EFRI 2-DARE grant 1542883, and by the Stanford SystemX Alliance. Authors are grateful for efforts of Jinshui Miao and Huiqin Zhang for metal deposition during sample preparation.

#### References

- 1. Das, S.; Robinson, J. A.; Dubey, M.; Terrones, H.; Terrones, M., Beyond Graphene: Progress in Novel Two-Dimensional Materials and Van Der Waals Solids. *Annual Review Of Materials Research* **2015**, *45*, 1-27.
- 2. Fiori, G.; Bonaccorso, F.; Iannaccone, G.; Palacios, T.; Neumaier, D.; Seabaugh, A.; Banerjee, S. K.; Colombo, L., Electronics Based on Two-Dimensional Materials. *Nature Nanotechnology* **2014**, *9*, 768-779.
- 3. Novoselov, K. S.; Falko, V. I.; Colombo, L.; Gellert, P. R.; Schwab, M. G.; Kim, K., A Roadmap for Graphene. *Nature* **2012**, *490*, 192-200.
- 4. Stanford, M. G.; Rack, P. D.; Jariwala, D., Emerging Nanofabrication and Quantum Confinement Techniques for 2D Materials Beyond Graphene. *Npj 2D Materials And Applications* **2018**, *2*, 20.
- 5. Brar, V. W.; Sherrott, M. C.; Jariwala, D., Emerging Photonic Architectures in Two-Dimensional Opto-Electronics. *Chemical Society Reviews* **2018**, *47*, 6824-6844.
- 6. Jariwala, D.; Marks, T. J.; Hersam, M. C., Mixed Dimensional Van Der Waals Heterostructures. *Nature Materials* **2017**, *16*, 170-181.
- 7. Jariwala, D.; Sangwan, V. K.; Lauhon, L. J.; Marks, T. J.; Hersam, M. C., Emerging Device Applications for Semiconducting Two-Dimensional Transition Metal Dichalcogenides. *ACS Nano* **2014**, *8*, 1102–1120.
- 8. Smyth, C. M.; Addou, R.; Mcdonnell, S.; Hinkle, C. L.; Wallace, R. M., Contact Metal–MoS<sub>2</sub> Interfacial Reactions and Potential Implications on MoS<sub>2</sub>-Based Device Performance. *The Journal Of Physical Chemistry C* **2016**, *120*, 14719-14729.
- 9. Domask, A. C.; Gurunathan, R. L.; Mohney, S. E., Transition Metal–MoS<sub>2</sub> Reactions: Review and Thermodynamic Predictions. *Journal Of Electronic Materials* **2015**, *44*, 4065-4079.
- 10. Liu, Y.; Guo, J.; Zhu, E.; Liao, L.; Lee, S.-J.; Ding, M.; Shakir, I.; Gambin, V.; Huang, Y.; Duan, X., Approaching the Schottky–Mott Limit in Van Der Waals Metal–Semiconductor Junctions. *Nature* **2018**, *557*, 696-700.
- 11. English, C. D.; Shine, G.; Dorgan, V. E.; Saraswat, K. C.; Pop, E., Improved Contacts To MoS<sub>2</sub> Transistors by Ultra-High Vacuum Metal Deposition. *Nano Letters* **2016**, *16*, 3824-3830.

- 12. Smithe, K. K. H.; Krayev, A. V.; Bailey, C. S.; Lee, H. R.; Yalon, E.; Aslan, Ö. B.; Muñoz Rojo, M.; Krylyuk, S.; Taheri, P.; Davydov, A. V.; Heinz, T. F.; Pop, E., Nanoscale Heterogeneities in Monolayer MoSe<sub>2</sub> Revealed by Correlated Scanning Probe Microscopy and Tip-Enhanced Raman Spectroscopy. *ACS Applied Nano Materials* **2018**, *1*, 572-579.
- 13. Kappera, R.; Voiry, D.; Yalcin, S. E.; Branch, B.; Gupta, G.; Mohite, A. D.; Chhowalla, M., Phase-Engineered Low-Resistance Contacts for Ultrathin MoS<sub>2</sub> Transistors. *Nature Materials* **2014**, *13*, 1128-1134.
- 14. Kang, J.; Liu, W.; Sarkar, D.; Jena, D.; Banerjee, K., Computational Study of Metal Contacts to Monolayer Transition-Metal Dichalcogenide Semiconductors. *Physical Review X* **2014**, *4*, 031005.
- 15. Allain, A.; Kang, J.; Banerjee, K.; Kis, A., Electrical Contacts to Two-Dimensional Semiconductors. *Nature Materials* **2015**, *14*, 1195-1205.
- 16. Jariwala, D.; Krayev, A.; Wong, J.; Robinson, E. A.; Sherrott, M. C.; Wang, S.; Liu, G.-Y.; Terrones, M.; Atwater, H. A., Nanoscale Doping Heterogeneity in Few-Layer WSe<sub>2</sub> Exfoliated onto Noble Metals Revealed by Correlated SPM and TERS Imaging. *2D Materials* **2018**, *5*, 035003.
- 17. Furchi, M. M.; Pospischil, A.; Libisch, F.; Burgdörfer, J.; Mueller, T., Photovoltaic Effect in an Electrically Tunable Van der Waals Heterojunction. *Nano Letters* **2014**, *14*, 4785-4791.
- 18. Koppens, F. H. L.; Mueller, T.; Avouris, P.; Ferrari, A. C.; Vitiello, M. S.; Polini, M., Photodetectors Based on Graphene, Other Two-Dimensional Materials and Hybrid Systems. *Nature Nanotechnology* **2014**, *9*, 780-793.
- 19. Baugher, B. W.; Churchill, H. O.; Yafang, Y.; Jarillo-Herrero, P., Optoelectronic Devices Based on Electrically Tunable P–N Diodes in a Monolayer Dichalcogenide. *Nature Nanotechnology* **2014**, *9*, 262-267.
- 20. Memaran, S.; Pradhan, N. R.; Lu, Z.; Rhodes, D.; Ludwig, J.; Zhou, Q.; Ogunsolu, O.; Ajayan, P. M.; Smirnov, D.; Fernández-Domínguez, A. I.; García-Vidal, F. J.; Balicas, L., Pronounced Photovoltaic Response from Multilayered Transition-Metal Dichalcogenides PN-Junctions. *Nano Letters* **2015**, *15*, 7532-7538.
- 21. Wong, J.; Jariwala, D.; Tagliabue, G.; Tat, K.; Davoyan, A. R.; Sherrott, M. C.; Atwater, H. A., High Photovoltaic Quantum Efficiency in Ultrathin Van der Waals Heterostructures. *ACS Nano* **2017**, *11*, 7230–7240.
- 22. Jariwala, D.; Davoyan, A. R.; Wong, J.; Atwater, H. A., Van Der Waals Materials for Atomically-Thin Photovoltaics: Promise and Outlook. *ACS Photonics* **2017**, *4*, 2692-2970.
- 23. Jariwala, D.; Davoyan, A. R.; Tagliabue, G.; Sherrott, M. C.; Wong, J.; Atwater, H. A., Near-Unity Absorption in Van der Waals Semiconductors for Ultrathin Photovoltaics. *Nano Letters* **2016**, *16*, 5482-5487.
- 24. Haigh, S. J.; Gholinia, A.; Jalil, R.; Romani, S.; Britnell, L.; Elias, D. C.; Novoselov, K. S.; Ponomarenko, L. A.; Geim, A. K.; Gorbachev, R., Cross-Sectional Imaging of Individual Layers and Buried Interfaces of Graphene-Based Heterostructures and Superlattices. *Nature Materials* **2012**, *11*, 764.
- 25. Desai, S. B.; Madhvapathy, S. R.; Amani, M.; Kiriya, D.; Hettick, M.; Tosun, M.; Zhou, Y.; Dubey, M.; Ager III, J. W.; Chrzan, D.; Javey, A., Gold-Mediated Exfoliation of Ultralarge Optoelectronically-Perfect Monolayers. *Advanced Materials* **2016**, *28*, 4053-4058.
- 26. Shim, J.; Bae, S.-H.; Kong, W.; Lee, D.; Qiao, K.; Nezich, D.; Park, Y. J.; Zhao, R.; Sundaram, S.; Li, X.; Yeon, H.; Choi, C.; Kum, H.; Yue, R.; Zhou, G.; Ou, Y.; Lee, K.; Moodera, J.; Zhao, X.; Ahn, J.-H.; Hinkle, C.; Ougazzaden, A.; Kim, J., Controlled Crack Propagation for Atomic Precision Handling of Wafer-Scale Two-Dimensional Materials. *Science* **2018**, *362*, 665-670.
- 27. Velický, M.; Donnelly, G. E.; Hendren, W. R.; Mcfarland, S.; Scullion, D.; Debenedetti, W. J. I.; Correa, G. C.; Han, Y.; Wain, A. J.; Hines, M. A.; Muller, D. A.; Novoselov, K. S.; Abruña, H. D.; Bowman, R.

- M.; Santos, E. J. G.; Huang, F., Mechanism of Gold-Assisted Exfoliation of Centimeter-Sized Transition-Metal Dichalcogenide Monolayers. *ACS Nano* **2018**, *12*, 10463-10472.
- 28. Chen, J.; Bailey, C. S.; Hong, Y.; Wang, L.; Cai, Z.; Shen, L.; Hou, B.; Wang, Y.; Shi, H.; Sambur, J.; Ren, W.; Pop, E.; Cronin, S. B., Plasmon-Resonant Enhancement of Photocatalysis on Monolayer WSe<sub>2</sub>. *ACS Photonics* **2019**, *6*, 787-792.
- 29. Smithe, K. K.; English, C. D.; Suryavanshi, S. V.; Pop, E., Intrinsic Electrical Transport and Performance Projections of Synthetic Monolayer MoS<sub>2</sub> Devices. *2D Materials* **2016**, *4*, 011009
- 30. Blakers, A. W.; Green, M. A.; Szpitalak, T., Surface Damage Caused by Electron-Beam Metallization of High Open-Circuit Voltage Solar Cells. *IEEE Electron Device Letters* **1984,** *5*, 246-247.
- 31. Haick, H.; Ambrico, M.; Ghabboun, J.; Ligonzo, T.; Cahen, D., Contacting Organic Molecules by Metal Evaporation. *Physical Chemistry Chemical Physics* **2004**, *6*, 4538-4541.
- 32. Mcmorrow, J. J.; Walker, A. R.; Sangwan, V. K.; Jariwala, D.; Hoffman, E.; Everaerts, K.; Facchetti, A.; Hersam, M. C.; Marks, T. J., Solution-Processed Self-Assembled Nanodielectrics on Template-Stripped Metal Substrates. *ACS Applied Materials & Interfaces* **2015**, *7*, 26360-26366.
- 33. Kumar, N.; Mignuzzi, S.; Su, W.; Roy, D., Tip-Enhanced Raman Spectroscopy: Principles and Applications. *EPJ Tech. And Instrum.* **2015**, *2*, 9.
- 34. Nie, Y.; Liang, C.; Zhang, K.; Zhao, R.; Eichfeld, S. M.; Cha, P.-R.; Colombo, L.; Robinson, J. A.; Wallace, R. M.; Cho, K., First Principles Kinetic Monte Carlo Study on The Growth Patterns of WSe<sub>2</sub> Monolayer. *2D Materials* **2016**, *3*, 025029.
- 35. Mignuzzi, S.; Pollard, A. J.; Bonini, N.; Brennan, B.; Gilmore, I. S.; Pimenta, M. A.; Richards, D.; Roy, D., Effect of Disorder on Raman Scattering of Single-Layer MoS<sub>2</sub>. *Physical Review B* **2015**, *91*, 195411.
- 36. Terrones, H.; Corro, E. D.; Feng, S.; Poumirol, J. M.; Rhodes, D.; Smirnov, D.; Pradhan, N. R.; Lin, Z.; Nguyen, M. A. T.; Elías, A. L.; Mallouk, T. E.; Balicas, L.; Pimenta, M. A.; Terrones, M., New First Order Raman-Active Modes in Few Layered Transition Metal Dichalcogenides. *Scientific Reports* **2014**, *4*, 4215.
- 37. Kang, D.-H.; Shim, J.; Jang, S. K.; Jeon, J.; Jeon, M. H.; Yeom, G. Y.; Jung, W.-S.; Jang, Y. H.; Lee, S.; Park, J.-H., Controllable Nondegenerate P-Type Doping of Tungsten Diselenide by Octadecyltrichlorosilane. *ACS Nano* **2015**, *9*, 1099-1107.
- 38. Agapov, R. L.; Sokolov, A. P.; Foster, M. D., Protecting TERS Probes from Degradation: Extending Mechanical and Chemical Stability. *J. Raman Spectrosc.* **2013**, *44*, 710-716.
- 39. Opilik, L.; Dogan, Ü.; Szczerbiński, J.; Zenobi, R., Degradation of Silver Near-Field Optical Probes and Its Electrochemical Reversal. *Applied Physics Letters* **2015**, *107*, 091109.
- 40. Michaelson, H. B., The Work Function of the Elements and its Periodicity. *Journal Of Applied Physics* **1977**, *48*, 4729-4733.
- 41. Fain, S. C.; Mcdavid, J. M., Work-Function Variation with Alloy Composition: Ag-Au. *Physical Review B* **1974**, *9*, 5099-5107.
- 42. Pandey, T.; Nayak, A. P.; Liu, J.; Moran, S. T.; Kim, J. S.; Li, L. J.; Lin, J. F.; Akinwande, D.; Singh, A. K., Pressure-Induced Charge Transfer Doping of Monolayer Graphene/MoS₂ Heterostructure. *Small* **2016**, *12*, 4063-4069.
- 43. Raider, S.; Berman, A., On The Nature of Fixed Oxide Charge. *Journal Of The Electrochemical Society* **1978**, *125*, 629-633.
- 44. Deal, B. E., Standardized Terminology For Oxide Charges Associated with Thermally Oxidized Silicon. *IEEE Transactions On Electron Devices* **1980**, *27*, 606-608.
- 45. Yeh, P.-C.; Jin, W.; Zaki, N.; Zhang, D.; Liou, J. T.; Sadowski, J. T.; Al-Mahboob, A.; Dadap, J. I.; Herman, I. P.; Sutter, P.; Osgood, R. M., Layer-Dependent Electronic Structure of an Atomically Heavy Two-Dimensional Dichalcogenide. *Physical Review B* **2015**, *91*, 041407.

- 46. Sahin, H.; Tongay, S.; Horzum, S.; Fan, W.; Zhou, J.; Li, J.; Wu, J.; Peeters, F. M., Anomalous Raman Spectra and Thickness-Dependent Electronic Properties of WSe2. *Physical Review B* **2013**, *87*, 165409.
- 47. Liu, H.; Jiao, L.; Xie, L.; Yang, F.; Chen, J.; Ho, W.; Gao, C.; Jia, J.; Cui, X.; Xie, M., Molecular-Beam Epitaxy of Monolayer and Bilayer WSe<sub>2</sub>: A Scanning Tunneling Microscopy/Spectroscopy Study and Deduction of Exciton Binding Energy. *2D Materials* **2015**, *2*, 034004.
- 48. Smyth, C. M.; Addou, R.; Mcdonnell, S.; Hinkle, C. L.; Wallace, R. M., WSe<sub>2</sub>-Contact Metal Interface Chemistry and Band Alignment under High Vacuum and Ultra High Vacuum Deposition Conditions. *2D Materials* **2017**, *4*, 025084.
- 49. Addou, R.; Smyth, C. M.; Noh, J.-Y.; Lin, Y.-C.; Pan, Y.; Eichfeld, S. M.; Fölsch, S.; Robinson, J. A.; Cho, K.; Feenstra, R. M., One Dimensional Metallic Edges in Atomically Thin WSe₂ Induced by Air Exposure. *2D Materials* **2018**, *5*, 025017.
- 50. Chen, C.-H.; Wu, C.-L.; Pu, J.; Chiu, M.-H.; Kumar, P.; Takenobu, T.; Li, L.-J., Hole Mobility Enhancement and P-Doping in Monolayer WSe2 by Gold Decoration. *2D Materials* **2014**, *1*, 034001.
- 51. Campbell, P. M.; Tarasov, A.; Joiner, C. A.; Tsai, M.-Y.; Pavlidis, G.; Graham, S.; Ready, W. J.; Vogel, E. M., Field-Effect Transistors Based on Wafer-Scale, Highly Uniform Few-Layer P-Type WSe<sub>2</sub>. *Nanoscale* **2016**, *8*, 2268-2276.
- 52. Liu, Y.; Stradins, P.; Wei, S.-H., Van der Waals Metal-Semiconductor Junction: Weak Fermi Level Pinning Enables Effective Tuning of Schottky Barrier. *Science Advances* **2016**, *2*, e1600069.

# TOC Graphic:

